RSC Advances

PAPER

View Article Online
View Journal | View Issue

Cite this: *RSC Adv.*, 2021, **11**, 30955

Ab initio study of alloying of MnBi to enhance the energy product

Tula R. Paudel, *[a] Bhubnesh Lama[a] and Parashu Kharel[b]

Received 29th June 2021
Accepted 7th September 2021

DOI: 10.1039/d1ra05007a

rsc.li/rsc-advances

High energy density magnets are preferred over induction magnets for many applications, including electric motors used in flying rovers, electric vehicles, and wind turbines. However, several issues related to cost and supply with state-of-the-art rare-earth-based magnets necessitate development of high-flux magnets containing low-cost earth-abundant materials. Here, by using first-principles density functional theory, we demonstrate the possibility of tuning magnetization and magnetocrystalline anisotropy of one of the candidate materials, MnBi, by alloying it with foreign elements. By using density functional theory in the high-throughput fashion, we consider the possibility of various metal and non-metal elements in the periodic table occupying empty sites of MnBi and found that MnBi-based alloys with Rh, Pd, Li, and O are stable against decomposition to constituent elements and have larger magnetization energy product compared to MnBi. Combined with other favorable properties of MnBi, such as high Curie temperature and earth abundancy of constituent elements, we envision the possibility of MnBi-based high-energy-density magnets.

MnBi, a member of Mn–A alloys, where A can be any element with 3+ oxidation state, such as Al, Ga, In, has potential to be a good magnet.[1–4] The compound has sizeable magnetocrystalline anisotropy energy (~0.163 meV uc^{-1} (ref. 5)), coercivity (~7 kOe at room temperature[6]), and energy product as large as 17 MGOe,[5] which are very attractive for magnet applications. Additionally, the compound has a large Curie temperature of 628 K,[1] and both coercivity and magnetocrystalline anisotropy increase with increasing temperature making it well suited for high-temperature applications. However, even with such favorable properties, the MnBi and MnBi-based compounds suffer from relatively low saturation magnetization.[7] Various ideas, including defect engineering,[2,8–13] exchange coupling with soft magnets,[7,10,14–21] and microstructural engineering,[22–26] have been tested to improve the energy products in these compounds. However, they have so far yielded mixed results. While most of the doping with various foreign elements and microstructure refinement has shown an increase of coercivity at the expense of magnetization,[2,3,8,27] Sn doping[3] is found to increase magnetization and magnetic anisotropy, leading to an increase in energy product.

In this manuscript, we test an alternative approach of alloying MnBi with foreign elements to enhance magnetization and magnetocrystalline anisotropy, leading to enhanced energy product $(BH)_{max}$. We use the high throughput density functional theory for screening suitable elements to form an alloy with MnBi. The structure of MnBi offers clues on why alloying may be possible in MnBi. The low-temperature phase of the MnBi crystallizes in hexagonal NiAs type structure (space group no. 194), as shown in Fig. 1. The lattice vectors of such a crystal are $A_1 = 1/2\ a\hat{x} + \sqrt{3}/2\ a\hat{y}$; $A_2 = 1/2\ a\hat{x} - \sqrt{3}/2\ a\hat{y}$ and $A_3 = c\hat{z}$, where a and c are lattice constants. Mn occupies 2a Wyckoff's positions with D_{3d} site symmetry: 0 and $(1/2A_3)$; Bi occupies 2c Wyckoff's positions with D_{3h} symmetry $(1/3A_1 + 2/3A_2 + 1/4A_3)$ and $(2/3A_1 + 1/3A_2 + 3/4A_3)$ while the other high symmetry Wyckoff's 2d positions: $(2/3A_1 + 1/3A_2 + 1/4A_3)$ and $(1/3A_1 + 2/3A_2 + 3/4A_3)$ are empty. We incorporate foreign elements to these sites and search for the elements that increase magnetization and coercivity. We consider two cases for each elemental (el) insertion. (i) Only one of two vacant sites is filled with foreign elements (half-filled case) such that effective concentration of alloy is 0.2/uc; the other half-filled configuration obtained by filling the rest vacant position is expected to behave similarly because of the similarity of lattice symmetry and the local environment surrounding the elements

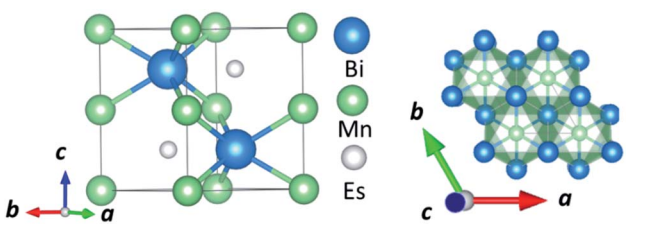

Fig. 1 Side view (left) and top view (right) of the NiAs type crystal structure of low-temperature phase MnBi.

[a]*Department of Physics, South Dakota School of Mines and Technology, Rapid City, SD 57701, USA. E-mail: tula.paudel@sdsmt.edu*

[b]*Department of Physics, South Dakota State University, Brookings, SD 57707, USA*

when placed in those positions, and (ii) both of the vacant sites are filled (full-filled case) such that effective concentration of alloy is 0.33/uc. Our strategy to find the suitable element for alloying is first to evaluate the formation energy of each alloy to find the stable one; second, determine saturation magnetization of stable alloys; and finally, calculate magnetic anisotropy energy of alloys that are stable and have magnetization larger than undoped MnBi.

For the stable alloy, the formation energy, ΔH, must be negative, which ascertains energy gain by alloying. The formation energy of the MnBi:el is evaluated as $\Delta H = E(\text{MnBi:el}) - E(\text{MnBi}) - E(\text{el})$. Here E(MnBi) and E(el) are energies of MnBi and energy of element, el. Similarly, E(MnBi:el) is the energy of the configuration of the alloy. We determine the energy of the alloy by comparing the energies of two configurations: first, ferromagnetic (FM) configuration in which magnetic moment of alloying elements aligns parallel to the magnetic moments of Mn; and second antiferromagnetic (AFM) configurations in which the magnetic moment of alloying element is aligned antiparallel to the magnetic moments of Mn. The calculated formation energy from these calculations is likely to be in the order of ~0.1 eV per formula unit, corresponding to ~10 kJ mol^{-1}.[28]

Fig. 2 shows the formation energy of the alloy with the various elements in the periodic table. Out of all those calculations, the stable alloys are the ones with the negative formation energy. In the half-filled case, only F and Pd doped alloys have negative formation energies. These are marked with light color in Fig. 2. Similarly, in the full-filled case, F, Y, and Rh doped alloys also have negative formation energies, indicating the alloys to be stable with respect to decomposition to the elemental phase. Other half-filled alloys with Rh, Pt, O, and Sc have formation energies less than 0.2 eV; these dopants only partially occupy these vacant sites. We calculate site occupancy $N_{\text{occ}}/N = \exp(-\Delta H/k_{\text{B}}T)$ at 500 K, where N is the number of available sites, k_{B} is the Boltzmann constant, and T is the temperature. We found that Rh, Pt, O, and Sc occupy 40%, 25%, 24%, and 2% of empty sites, respectively. Similarly, full-filled MnBi alloys with La, Ca, and Pt have slightly positive formation energy (<0.2 eV) and only partially occupy the empty sites: La occupies 6%, Ca occupies 9%, and Pt occupies 23% of the empty sites. When $\Delta H > 0.2$ eV occupation of interstitial sites of MnBi reduces to less than 1%. While ternary phase diagrams of many of these elements with MnBi are unavailable, experimental studies including Mn–Rh–Bi ternary phase diagram shows the presence of various phases including $Mn_{1.05}Rh_{0.02}Bi$,[29] $Mn_{0.8}RhBi_{0.2}$,[30] and $Mn_5Rh_6Bi_{18}$ and $MnRhBi_3$ (ref. 31) consistent with our prediction of high solubility of Rh in MnBi.

All the alloys with negative formation energy are found to have a larger volume compared to that of MnBi. The lattice volume increases, but modestly, according to the increase in the atomic radius.[32] The smallest volume increase is observed in F (1%), and the largest volume increase is observed in the case of Y (42%). Volume increases more in the full-filled than half-filled case; however, the increase is not linear; for example, the volume increase of full-filled MnBiRh is ~19%, whereas that of half-filled $MnBiRh_{1/2}$ is ~14%. This nonlinear increase in volume indicates additional hybridization between the alloying elements and MnBi while both empty sites are occupied. Despite the increase in volume, the volume formation, which is defined in a similar way as the formation energy, $\Delta V_{\text{F}} = V(\text{MnBi:}n\text{el}) - (V_{\text{MnBi}} - nV_{\text{el}})$, where n is number of doped elements, Ve_{l} is volume of doped element, and V_{MnBi} is the volume of MnBi, is generally negative (except for MnBi:Pt) as shown in Table 1. The negative ΔV_{F} also indicates bonding of the alloying elements with Mn and Bi in MnBi.

Having found the stable alloys, we next analyze their magnetic properties. Table 1 shows changes in magnetization with respect to the $3.54\mu_{\text{B}}$ per Mn of bulk MnBi. Here magnetization per Mn atom is determined by dividing total magnetization density that minimize total energy of system by number of Mn atoms, assuming magnetism is mostly carried by Mn atoms. Out of the alloys with negative formation energy,

1 IA																17 VIIA
1.71 H 3.32	2 IIA											13 IIIA	14 IVA	15 VA	16 VIA	H
0.64 Li -1.27	1.42 Be 2.77											2.24 B 6.54	4.75 C 9.42	3.08 N 5.35	0.1 O -0.72	-1.33 F -2.7
2.65 Na 0.94	1.52 Mg 0.9	3 IIIB	4 IVB	5 VB	6 VIB	7 VIIB	8	9 VIIIB	10	11 IB	12 IIB	1.29 Al 2.37	1.9 Si 3.12	3.47 P 2.54	1.72 S 1.84	1.81 Cl 2.02
2.77 K 3.23	0.72 Ca 0.1	0.16 Sc -0.74	0.39 Ti 0.73	0.9 V 1.75	1.19 Cr 2.27	1.15 Mn 2.09	0.97 Fe 2.35	0.41 Co 1.37	1.12 Ni 1.03	0.75 Cu 1.33	2.5 Zn 1.68	1.31 Ga 1.74	1.73 Ge 2.87	1.83 As 2.31	1.86 Se 1.95	2.55 Br 2.99
3.81 Rb 4.98	1.5 Sr 0.88	0.68 Y -0.24	0.7 Zr 0.86	1.35 Nb 2.89	1.76 Mo 4.0	Tc	1.94 Ru 1.83	0.04 Rh -0.02	-0.06 Pd -0.46	1.11 Ag 1.67	1.62 Cd 2.42	1.93 In 2.65	2.12 Sn 2.78	2.67 Sb 2.6	4.64 Te 2.79	3.64 I 4.58
	2.49 Ba 2.72	1.11 La 0.12	0.97 Hf 1.42	1.79 Ta 4.03	2.59 W 5.65	2.31 Re 4.91	1.85 Os 3.76	1.88 Ir 1.28	0.09 Pt 0.06	0.95 Au 0.94	Hg	Tl	2.58 Pb 3.24	4.47 Bi 3.2	Po	At

ΔH ($MnBiel_{1/2}$)
Dopants
ΔH (MnBiel)

Fig. 2 The formation energy (eV) of the MnBi alloy with the various elements. The numbers above and below each element in the box represent the formation energy, ΔH, of half-filled (MnBi:$el_{1/2}$) and full filled (MnBi:el) alloy with the element (el). The isolated box shows the legend. The highlighted elements form a stable alloy with MnBi.

Table 1 Change in saturation magnetization (ΔM), anisotropy (ΔAE), volume formation (ΔV_F), c/a, energy difference ($\Delta E = E_{FM} - E_{AFM}$) between antiferromagnetic (AFM) and ferromagnetic (FM) configurations, estimated Curie temperature (T_c) and change in energy product, $\Delta(BH)_{max}$ (%) as a function of alloying elements (el) in half-filled MnBi:$el_{1/2}$ and full-filled MnBi:el alloys

Case	ΔM (%)	ΔAE (MJ m^{-3})	ΔV (%)	ΔV_F (Å^3)	c/a	ΔE (eV)	T_c (K)	$\Delta(BH)_{max}$ (%)
MnBi	0	0			1.33	−0.3	580	0
MnBi:Li	9	4	18	−23.26	1.24	−0.1	190	18
MnBI:O	9	5	8	−19.62	1.05	−0.29	555	18
MnBi:$F_{1/2}$	−2		1.0	−18.23	1.28			
MnBi:F	−7		1.5	−19.62	1.27			
MnBi:$Sc_{1/2}$	−9		26	−0.10	1.18			
MnBi:Sc	−2		36	−16.15	1.18			
MnBi:Y	−7		42	−26.15	1.17			
MnBi:$Rh_{1/2}$	8	3.0	13	−1.53	1.33	−0.27	522	16
MnBi:Rh	14	0.92	19	−10.80	1.21	−0.16	312	32
MnBi:$Pd_{1/2}$	9	20.7	18	−0.46	1.33	−0.24	457	18
MnBi:Pd	14	0.33	27	−5.98	1.22	−0.17	327	30
MnBi:$Pt_{1/2}$	10	6.37	19	2.74	1.25	−0.23	442	21
MnBi:Pt	10	4.79	20	−13.04	1.20	−0.22	417	21

alloying with F, Sc, Y reduces the net magnetization, where alloying with Li, O, Rh, Pd, and Pt increases net magnetization by up to 14% compared to the undoped case. In the case of F doping, F-p orbital hybridizes strongly with Bi-p orbitals (Fig. 3c), which couples to Mn-d orbitals antiferromagnetically like that in bulk MnBi, thereby reducing the net moment. In the case of Sc and Y, their 3d-states, as shown in Fig. 3d and e, mainly lie in the conduction band; thus, they hybridize with Mn minority d-states, inducing small moments in themselves and reducing moments in Mn, and the moments in Y and Sc couple antiferromagnetically with Mn moments further reducing the overall magnetizations.

Alloying with Rh, Pd, Pt increases the net magnetization of the system. 4d orbitals of the Rh (Fig. 3f) and Pd (Fig. 3g) and 5d orbitals of the Pt (Fig. 3h) lies mainly in the valence band and hybridize strongly with the majority spin-channel of Mn, which induces small magnetic moments on themselves and enhances magnetic moments on Mn. These moments on Rh, Pd, and Pt, however, couple ferromagnetically with Mn moments, which is opposite to interaction between Mn at the regular sites and interstitial sites, which couples antiferromagnetically,[33,34] or interaction between Sc, Y in interstitial sites and Mn at regular sites, as we discussed previously. The difference comes from the large exchange splitting of Mn-d bands leading to almost no interaction between electrons with different spins located at the different sites. However, in Rh, Pd, and Pt, even though intra-atomic exchange interaction leads to d-orbitals splitting according to spin like that in Mn, the splitting is much smaller. As a result, bands corresponding to both spin channels are occupied though there is a slight shift between them, which results in a small magnetic moment. Additionally, they have a significant overlap with Mn d-orbitals occupied by the majority spin channel, resulting in ferromagnetic direct exchange.

Alloying group II elements like Li and O also increases overall magnetization. The s-states of Li and p-states of O lie on the opposite side of the Fermi level: The O-p states lie primarily in the valence band as shown in Fig. 3j, while Li-s states lie in the conduction band as shown in Fig. 3i. As a result, the hybridization between Li-s states and Mn-d states, and O-p and Mn-d states is spin-dependent; the oxygen states hybridize mostly with the Mn-d majority states, while Li-s states hybridize mostly with Mn-d minority states leading to the enhancement of Mn moments and development of small moments in Li and O themselves. The magnetic moments of Li and O also couple ferromagnetically because of direct exchange with Mn moments and help increasing overall magnetization. We verify this hypothesis by explicitly comparing the energy of the system with the moments of Mn and moments of Li and O coupling ferromagnetically and antiferromagnetically and found that the ferromagnetically coupled system has lower energy. Using the energy difference $\Delta E = E_{FM} - E_{AFM}$ we estimate the Curie temperature in the mean-field approximations by using $T_c = \Delta E/3$.[34] For the bulk MnBi, we calculate $\Delta E = 150$ meV per Mn and $T_c \approx 580$ K, which is reasonably close to extrapolated experimental value of 775 K;[35] the structural transition at 628 K hinder measuring real T_c of MnBi. Using the same approach, we evaluate the T_c of stable MnBi alloys with enhanced magnetizations. The second to last column of the Table 1 shows the calculated results, which shows that T_c reduces in general upon doping. This is consistent with the fact that upon doping antiferromagnetic magnetic exchange J_1 between nearest neighbor Mn-atoms in c-directions[34] increases because of enhancement of volume, reduction of c/a ratio and increase in orbital overlap. The other exchange parameters related with second (J_2), third (J_3), fourth (J_4), fifth (J_5) and sixth (J_6) nearest neighbor Mn atoms are ferromagnetic and smaller than J_1.[5] With the increase of J_1 the net exchange $J = 2J_1 + 6J_2 + 12J_3 + 2J_4 + 2J_5 + 2J_6$ can be expected to decrease and along with it the T_c, as $T_c = \frac{3}{2k_B}J$,[5] while the other J_s are also expected to be affected upon alloying, their large coefficients will remain same so that J remains negative and alloy still is ferromagnetic.

Next, we calculate change in magnetic anisotropy energy MAE, ΔMAE = MAE(MnBi:el/$el_{1/2}$) − MAE(MnBi), in stable

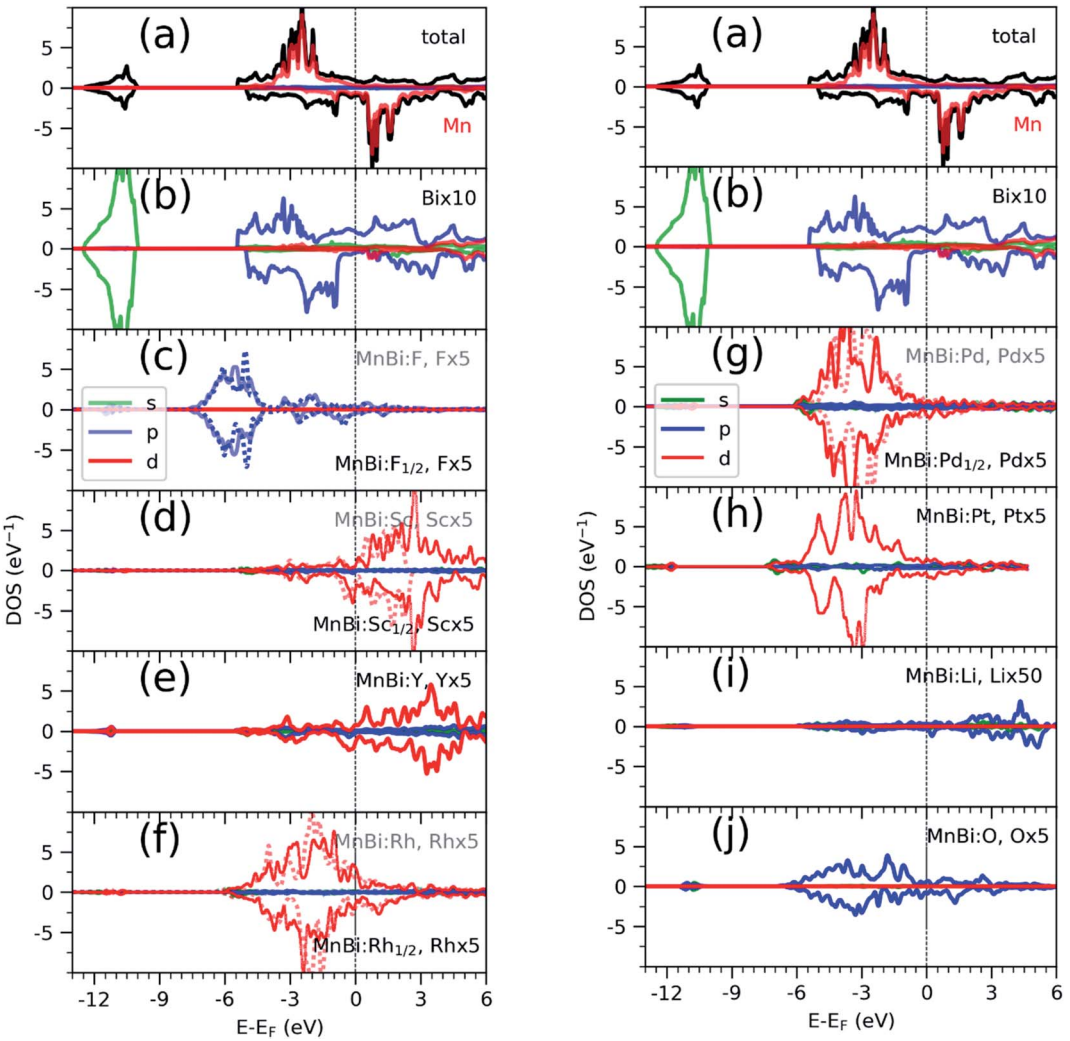

Fig. 3 Density of states (DOS) of MnBi total (black) projected to Mn atoms (a), projected to Bi atoms (b), and projected to various alloying elements (el) (c) to (j) resolved according to spin: majority in positive axis and minority in negative axis and orbitals: color red, blue, and green corresponds to d, p and s orbitals respectively. In the cases (F, Rh and Pd), where both half-filled and full-filled alloys are stable, the DOS of element in full-filled alloy is shown with dotted line in the background of solid line that corresponds to DOS of the element in half-filled case. el × *x*, where *x* is 5 or 10 in (c–f) and (g–j) corresponds to the enlargement factor for DOS for better visualization.

alloys with magnetization larger than that of bulk MnBi. MAE is computed by taking the energy difference between the system with magnetization pointing along [100] direction and the system with magnetization pointing along [001] direction, MAE $= E(M\|[100]) - E(M\|[001])$. The results in Table 1 show that anisotropy energy increases upon alloying compared to MnBi ($\sim$1 MJ m^{-3}) in all cases. Since the anisotropy energy $E = K_1 \sin^2\theta + K_2 \sin^4\theta$, where θ is the angle between easy axis [001] and the direction of magnetization, and $K_2 \ll K_1$, ΔMAE roughly corresponds to change in K_1. We note that magnetization of MnBi alloy with Rd and $Pd_{1/2}$ points along [001] direction, similar to the bulk MnBi, the magnetization of MnBi alloyed with Li, O, Pd, and Pt changes to in-plane [100] direction. Qualitatively, such changes in MAE and easy axis are related to subtle changes in band distribution near the Fermi level and may require separate detailed investigation. The magnetic anisotropy is a relativistic effect driven by spin–orbit coupling (SOC). As the spin–orbit coupling energy is much smaller than the bandwidth of Mn-3d states, perturbative expansion of energy can be used to explain the spin–orbit coupling effect. The lowest non-zero correction to the energy in such expansion includes the term proportional to $1/(E_{\mathrm{unocc}} - E_{\mathrm{occ}})$ where $E_{\mathrm{occ(unocc)}}$ is the energy of occupied (unoccupied) state around Fermi energy for each *k*-points[36] in the Brillouin zone. While the system is metallic, $E_{\mathrm{unocc}} - E_{\mathrm{occ}}$ remains finite for the majority of the *k*-points and the SOC induced change in energy does not diverge. The non-zero DOS of alloying elements near the Fermi level indicates the possibility of such changes near Fermi levels.

Finally, we estimate the theoretical value of maximum energy product $(BH)_{\max}$ assuming applied field H much smaller than magnetization, M. In this approximation, magnetic induction field $B = 4\pi M$ in CGS units, and remanent magnetization, $M_r = M_s$, saturation magnetization when the magnetic hysteresis loop is almost rectangular. The $(BH)_{\max} = B_r^2/4$,

where the remnant field $B_r = 4\pi M_r = 4\pi M_s$.[37] The formula allows us to estimate the energy-product using only the intrinsic properties such as actual magnetization (emu cm^{-3}) and homogeneous sample without using coercivity that relies on the extrinsic factors such as shape and size of the sample. The last column of Table 1 shows the calculated percentage change in energy product to calculated energy product of 20 MGOe, which is similar to the value of 17 MGOe[38,39] measured experimentally. The energy product enhances when MnBi is alloyed with Pd, Pt, Rh, Li, and O per the change in magnetizations.

In summary, we used the first-principles density functional theory to find an alloy with the increased magnetization and anisotropy. We predict MnBi alloy with Pd, Pt, Rh, Li, and O are stable against decomposition to constituent elements and have larger magnetization and anisotropy compared to MnBi and have a high energy product. Magnetic easy axis of MnBi alloy with $Pd_{1/2}$ and Rh remains the same as bulk MnBi and lies out-of-plane direction, while the magnetic-easy-axis of MnBi alloy with Li, O, Pd and Pt lie in-plane. Pd can rotate the magnetic-easy-axis[40] from in-plane to out-of-plane depending upon the percentage of Pd that would be incorporated in MnBi. We anticipate this comprehensive study of MnBi alloy spurs more theoretical and experimental study. We note that the alloying of these elements with MnBi may require non-equilibrium growth methods as their formation energies are relatively small.

Computational methods

We employ the projected augmented wave (PAW)[41] method for the electron-ion potential and the gradient density approximation (GGA) for exchange–correlation potential, as implemented in the Vienna *ab initio* simulation package (VASP)[42,43] with the recommended set of pseudopotentials.[44] The calculations are carried out using the kinetic energy cutoff of 340 eV and $6 \times 6 \times 1$ *k*-point mesh for Brillouin zone integration of pseudocubic unit cells. The *k*-points are scaled according to size. We fully relax ionic coordinates with the force convergence limit of 0.001 eV per atom. For the anisotropy calculations, we include an additional onsite Coulomb interaction Hubbard (*U–J*) parameter of 3 eV to Mn-3d states so that the sign of magnetocrystalline of bulk MnBi is consistent with the experiments and includes spin–orbit coupling terms explicitly.

Data availability

The data that support the findings of this are available from the corresponding author upon reasonable request.

Conflicts of interest

There are no conflicts to declare.

Acknowledgements

This work was supported by South Dakota-NASA EPSCoR Research Initiation grant no 80NSSC19M0063. Computations were performed utilizing the Holland Computing Center at the University of Nebraska, Lincoln, and the Gamow Computing Cluster at the Department of Physics, South Dakota School of Mines and Technology. The authors acknowledge discussion with Alex Leary, Research Materials Engineer at the NASA Glenn Research Center, Cleveland, OH.

References

1 P. Kharel, *et al.*, Transport spin polarization of high Curie temperature MnBi films, *Phys. Rev. B: Condens. Matter Mater. Phys.*, 2011, **83**, 1–6.
2 P. Kharel, *et al.*, Structural, magnetic, and electron transport properties of MnBi:Fe thin films, *J. Appl. Phys.*, 2012, **111**, 07E326.
3 W. Zhang, *et al.*, High energy product of MnBi by field annealing and Sn alloying, *APL Mater.*, 2019, **7**(12), 121111.
4 V. N. Antonov and V. P. Antropov, Low-temperature MnBi alloys: Electronic and magnetic properties, constitution, morphology and fabrication (Review article), *Low Temp. Phys.*, 2020, **46**, 3–32.
5 J. Park, *et al.*, Electronic Structure and Maximum Energy Product of MnBi, *Metals*, 2014, **4**, 455–464.
6 J. Cao, *et al.*, Microstructure and magnetic properties of MnBi alloys with high coercivity and significant anisotropy prepared by surfactant assisted ball milling, *J. Magn. Magn. Mater.*, 2019, **473**, 505–510.
7 Y. L. Ma, *et al.*, Preparation and magnetic properties of MnBi-based hard/soft composite magnets, *J. Appl. Phys.*, 2014, **115**, 19–22.
8 R. F. Sabiryanov and S. S. Jaswal, Magneto-optical properties of MnBi doped with Cr, *J. Appl. Phys.*, 1999, **85**, 5109–5111.
9 A. Sakuma, Y. Manabe and Y. Kota, First Principles Calculation of Magnetocrystalline Anisotropy Energy of MnBi and MnBi 1- x Sn x, *J. Phys. Soc. Jpn.*, 2013, **82**, 073704.
10 V. V. Ramakrishna, S. Kavita, R. Gautam, T. Ramesh and R. Gopalan, Investigation of structural and magnetic properties of Al and Cu doped MnBi alloy, *J. Magn. Magn. Mater.*, 2018, **458**, 23–29.
11 P. Rani, A. Taya and M. K. Kashyap, Enhancement of magnetocrystalline anisotropy of MnBi with Co interstitial impurities, *AIP Conf. Proc.*, 2018, **1942**, 130033.
12 Y. Yang, *et al.*, Effects of Ga-doping on the microstructure and magnetic properties of MnBi alloys, *J. Alloys Compd.*, 2018, **769**, 813–816.
13 K. Anand, N. Christopher and N. Singh, Evaluation of structural and magnetic property of Cr-doped MnBi permanent magnet material, *Appl. Phys. A*, 2019, **125**, 870.
14 R. Skomski and J. M. D. Coey, Giant energy product in nanostructured two-phase magnets, *Phys. Rev. B: Condens. Matter Mater. Phys.*, 1993, **48**, 15812–15816.
15 R. Skomski and J. M. D. Coey, Exchange Coupling and Energy Product in Random Two-Phase Aligned Magnets, *IEEE Trans. Magn.*, 1994, **30**, 607–609.
16 R. Skomski, Aligned two-phase magnets: Permanent magnetism of the future? (invited), *J. Appl. Phys.*, 1994, **76**, 7059–7064.

17 H. Zeng, J. Li, J. P. Liu, Z. L. Wang and S. Sun, Exchange-coupled nanocomposite magnets by nanoparticle self-assembly, *Nature*, 2002, **420**, 395–398.
18 X. Xu, *et al.*, Magnetic self-assembly for the synthesis of magnetically exchange coupled MnBi/Fe-Co composites, *J. Solid State Chem.*, 2015, **231**, 108–113.
19 Q. Dai, M. Asif warsi, J. Q. Xiao and S. Ren, Solution processed MnBi-FeCo magnetic nanocomposites, *Nano Res.*, 2016, **9**, 3222–3228.
20 T. R. Gao, *et al.*, Large energy product enhancement in perpendicularly coupled MnBi/CoFe magnetic bilayers, *Phys. Rev. B*, 2016, **94**, 2–6.
21 S. K. Jain, B. L. Chittari and V. Kumar, Optimum thickness of soft magnetic phase in FePt/FeCo permanent magnet superlattices with high energy product and large magnetic anisotropy energy, *AIP Adv.*, 2016, **6**(2), 025027.
22 F. Yin, N. Gu, T. Shigematsu and N. Nakanishi, Sintering formation of low temperature phase MnBi and its disordering in mechanical milling, *J. Mater. Sci. Technol.*, 1996, **12**, 335–341.
23 J. B. Yang, *et al.*, Anisotropic nanocrystalline MnBi with high coercivity at high temperature, *Appl. Phys. Lett.*, 2011, **99**, 2011–2014.
24 H. Kronmüller, J. B. Yang and D. Goll, Micromagnetic analysis of the hardening mechanisms of nanocrystalline MnBi and nanopatterned FePt intermetallic compounds, *J. Phys.: Condens. Matter*, 2014, **26**, 064210.
25 E. Céspedes, *et al.*, High coercive LTP-MnBi for high temperature applications: From isolated particles to film-like structures, *J. Alloys Compd.*, 2017, **729**, 1156–1164.
26 Y. L. Huang, Z. Q. Shi, Y. H. Hou and J. M. Cao, improved magnetic properties, and recoil loops characteristics for MnBi alloys, *J. Magn. Magn. Mater.*, 2019, **485**, 157–164.
27 P. Kharel, R. Skomski, R. D. Kirby and D. J. Sellmyer, Structural, magnetic and magneto-transport properties of Pt-alloyed MnBi thin films, *J. Appl. Phys.*, 2010, **107**, 66.
28 V. Stevanović, S. Lany, X. Zhang and A. Zunger, Correcting density functional theory for accurate predictions of compound enthalpies of formation: Fitted elemental-phase reference energies, *Phys. Rev. B: Condens. Matter Mater. Phys.*, 2012, **85**, 115104.
29 V. Taufour, *et al.*, Structural and ferromagnetic properties of an orthorhombic phase of MnBi stabilized with Rh additions, *Phys. Rev. Appl.*, 2015, **4**, 1–9.
30 J. C. Suits, Ferromagnetism in Bi- and Te-substituted MnRh, *IBM J. Res. Dev.*, 1975, **19**, 422–423.
31 P. Kainzbauer, K. W. Richter, H. S. Effenberger, M. C. J. Marker and H. Ipser, Single-crystal structure determination of two new ternary bismuthides: Rh 6 Mn 5 Bi 18 and RhMnBi 3, *Acta Crystallogr., Sect. C: Struct. Chem.*, 2018, **74**, 863–869.
32 E. Clementi, D. L. Raimondi and W. P. Reinhardt, Atomic screening constants from SCF functions. II. Atoms with 37 to 86 electrons, *J. Chem. Phys.*, 1967, **47**, 1300–1307.
33 A. E. Taylor, *et al.*, Influence of interstitial Mn on magnetism in the room-temperature ferromagnet $Mn^{1+\delta}Sb$, *Phys. Rev. B: Condens. Matter Mater. Phys.*, 2015, **91**, 1–11.
34 T. J. Williams, *et al.*, Extended magnetic exchange interactions in the high-temperature ferromagnet MnBi, *Appl. Phys. Lett.*, 2016, **108**(19), 192403.
35 X. Guo, X. Chen, Z. Altounian and J. O. Ström-Olsen, Temperature dependence of coercivity in MnBi, *J. Appl. Phys.*, 1993, **73**, 6275–6277.
36 P. Bruno, Tight-binding approach to the orbital magnetic moment and magnetocrystalline anisotropy of transition-metal monolayers, *Phys. Rev. B: Condens. Matter Mater. Phys.*, 1989, **39**, 865–868.
37 J. M. D. Coey, *Magnetism and Magnetic Materials*, Cambridge University Press, 2001, DOI: 10.1017/CBO9780511845000.
38 R. G. Pirich, J. David and J. Larson, *US Pat.*, 4784703, 19, 1988.
39 W. Zhang, P. Kharel, S. Valloppilly, L. Yue and D. J. Sellmyer, High-energy-product MnBi films with controllable anisotropy, *Phys. Status Solidi B*, 2015, **252**, 1934–1939.
40 V. G. Myagkov, *et al.*, High rotatable magnetic anisotropy in MnBi thin films, *JETP Lett.*, 2017, **105**, 651–656.
41 P. E. Blöchl, Projector augmented-wave method, *Phys. Rev. B: Condens. Matter Mater. Phys.*, 1994, **50**, 17953–17979.
42 G. Kresse and J. Furthmüller, Efficient iterative schemes for ab initio total-energy calculations using a plane-wave basis set, *Phys. Rev. B: Condens. Matter Mater. Phys.*, 1996, **54**, 11169–11186.
43 G. Kresse, From ultrasoft pseudopotentials to the projector augmented-wave method, *Phys. Rev. B: Condens. Matter Mater. Phys.*, 1999, **59**, 1758–1775.
44 Recommended potentials for DFT calculations, https://www.vasp.at/wiki/index.php/Available_PAW_potentials.